Original Article

High-resolution harmonic motion imaging (HR-HMI) for tissue biomechanical property characterization

Teng Ma, Xuejun Qian, Chi Tat Chiu, Mingyue Yu, Hayong Jung, Yao-Sheng Tung, K. Kirk Shung, Qifa Zhou

Department of Biomedical Engineering, NIH Recourse Center on Medical Ultrasonic Transducer Technology, University of Southern California, Los Angeles, California, USA

Correspondence to: Qifa Zhou. Research Professor in Biomedical Engineering, NIH Resource Center on Medical Ultrasonic Transducer Technology, University of Southern California, 136 DRB, 1042 Downey Way, Los Angeles, CA 90089-1111, USA. Email: qifazhou@usc.edu.

Background: Elastography, capable of mapping the biomechanical properties of biological tissues, serves as a useful technique for clinicians to perform disease diagnosis and determine stages of many diseases. Many acoustic radiation force (ARF) based elastography, including acoustic radiation force impulse (ARFI) imaging and harmonic motion imaging (HMI), have been developed to remotely assess the elastic properties of tissues. However, due to the lower operating frequencies of these approaches, their spatial resolutions are insufficient for revealing stiffness distribution on small scale applications, such as cancerous tumor margin detection, atherosclerotic plaque composition analysis and ophthalmologic tissue characterization. Though recently developed ARF-based optical coherence elastography (OCE) methods open a new window for the high resolution elastography, shallow imaging depths significantly limit their usefulness in clinics.

Methods: The aim of this study is to develop a high-resolution HMI method to assess the tissue biomechanical properties with acceptable field of view (FOV) using a 4 MHz ring transducer for efficient excitation and a 40 MHz needle transducer for accurate detection. Under precise alignment of two confocal transducers, the high-resolution HMI system has a lateral resolution of 314 μm and an axial resolution of 147 μm with an effective FOV of 2 mm in depth.

Results: The performance of this high resolution imaging system was validated on the agar-based tissue mimicking phantoms with different stiffness distributions. These data demonstrated the imaging system's improved resolution and sensitivity on differentiating materials with varying stiffness. In addition, *ex vivo* imaging of a human atherosclerosis coronary artery demonstrated the capability of high resolution HMI in identifying layer-specific structures and characterizing atherosclerotic plaques based on their stiffness differences.

Conclusions: All together high resolution HMI appears to be a promising ultrasound-only technology for characterizing tissue biomechanical properties at the microstructural level to improve the image-based diseases diagnosis in multiple clinical applications.

Keywords: Elastography; high frequency ultrasound; biomechanical properties; medical imaging; acoustic radiation force (ARF); harmonic motion imaging (HMI)

Submitted Oct 23, 2014. Accepted for publication Oct 31, 2014.
doi: 10.3978/j.issn.2223-4292.2014.11.27
View this article at: http://dx.doi.org/10.3978/j.issn.2223-4292.2014.11.27

Introduction

Tissue biomechanical properties, highly correlated to the tissue pathophysiological change such as inflammation, aging and tumorous process, are commonly used by clinicians to identify the diseased tissue and determine the disease states (1). For example, cancerous lesions are often times stiffer than the surrounding tissue and the mechanical properties of atherosclerosis plaques are linked to the vulnerability of the plaques (2,3). Elastography has been developed in the past two decades to quantitatively map the tissue biomechanical properties onto the structural image by measuring the tissue deformation amplitude under internally or externally mechanical excitation (4). Among several elastographical imaging techniques being investigated, ultrasound elastography is the most commonly used method clinically (5). In traditional ultrasound elastography, the palpation method uses a compressional force to the tissue via a plate or the transducer itself and the induced deformation is measured to assess the tissue's elasticity (4). However, the heavy dependence on the physicians' experiences and skills limits the clinical use of this technique. As a more reliable substitute for the palpation method, acoustic radiation force (ARF), generated during the propagation and attenuation of ultrasonic wave within the tissue, has been used to deform the tissue in a more accurate and controllable manner (6). Many ARF-based imaging techniques have been investigated for tissue elasticity characterization, such as acoustic radiation force impulse (ARFI) imaging (7), vibroacoustic imaging (8), supersonic shear wave imaging (SSI) (9), shear wave elastography (SWE) (10) and harmonic motion imaging (HMI) (11-14). Nonetheless, the spatial resolution of the elastography images in most of these studies is significantly limited by the low operating frequency (<15 MHz), which makes it difficult to characterize the tissue biomechanical properties at the microstructural level (15,16). Therefore, a high resolution elastography is desired to access the tissue biomechanical properties in a small scale so as to improve the diagnosis of diseases such as the tumor margin detection, atherosclerosis plaque composition analysis and ophthalmologic tissue characterization. In 2007, phase sensitive or phase resolved optical coherence elastography (OCE), an approach based on the measurement of phase changes in optical coherence tomography (OCT) images, has been developed to generate the microstrain map of tissue subjected to a dynamic compression in real time (17). Later, by combining ARF-based excitation method and OCE-based detection method, acoustic radiation force optical coherence elastography (ARF-OCE) was developed. Based on the measurement of the vibrational movement induced by dynamic ultrasound waves in longitudinal direction, 3D elasticity maps can be obtained with both high temporal and spatial resolutions (18,19). Similarly, shear wave optical coherence elastography (SW-OCE) is another attempt to integrate ARF and OCE to facilitate the high-resolution shear modulus map of tissues by tracking the propagating shear wave in the transverse direction (20). The recently developed resonant ARF-OCE imaging technique utilizes the concept of mechanical resonant frequency and HMI to characterize and identify tissues of different types by sweeping different ARF modulation frequencies and measuring the frequency-dependent displacements, which provides an additional contrast to the ARF-OCE technique (21). Although ARF-based mechanical excitation capitalizes the advantage of providing the accurate remote palpation, the OCE-based detection mechanism still suffers from the shallow depth penetration, which greatly limits the clinical practicality of these OCE techniques. Given that there is a significant gap between ultrasonic elastography and OCE on the imaging resolution and depth penetration, Shih et al. improved the resolution of ARFI imaging by using a dual-element ultrasonic transducer to accomplish the low frequency (11 MHz) ARF excitation and high frequency (48 MHz) ultrasonic detection. The increased detection frequency has significantly improved the spatial resolutions when compared with the traditional ARFI imaging operating in the low frequency range (22). However, due to the restricted confocal region of dual elements transducers with large frequency difference, this method requires time-consuming multiple axial depths scan (B/D scan) to generate a 2 mm imaging field of view (FOV).

The aim of this study is to develop a high-resolution harmonic motion imaging (HR-HMI) technique for characterizing tissue biomechanical properties in a small scale. A focused 4 MHz large aperture ring shape transducer for generating effective ARF excited displacements and a 40 MHz unfocused small aperture needle transducer for detecting the ARF induced vibrational displacements were designed and fabricated in this study. The ring transducer and needle transducer were carefully arranged in a confocal configuration to maintain an improved sensitivity and a more satisfactory FOV during the experiments. Imaging tests on both a tissue mimicking phantom and an *ex vivo* human atherosclerosis coronary cadaver sample were carried out to evaluate the performance of this imaging system. The experimental results suggest that this ultrasound-only technique offers a more reliable capability of differentiating tissue biomechanical properties with promising translational

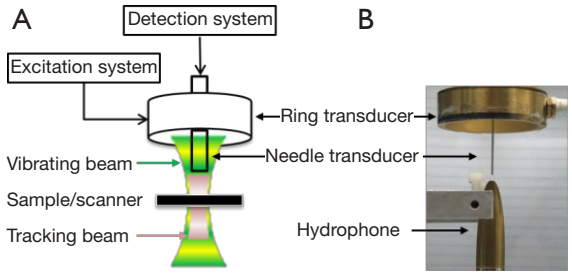

Figure 1 (A) Schematic of experimental setup; (B) photograph of arrangement of ultrasonic transducers.

Table 1 Design parameters and measured properties of transducers

Properties	Transducer	
	Excitation transducer	Detection transducer
Material	PZT ceramics	PMN-PT single crystal
Shape	Focused ring-shape	Unfocused square-shape
Center frequency	4 MHz	40 MHz
Aperture size	30 mm OD and 10 mm ID	0.56 mm side length
Focal depth	30 mm	2.3 mm
Lateral focal zone	0.36 mm (–6 dB)	0.31 mm (–3 dB)
Axial focal zone	2 mm (–6 dB)	4.3 mm (–3 dB)

PZT, Pb (Zr, Ti)O_3; PMN-PT, Pb($Mg_{1/3}Nb_{2/3}$)-$PbTiO_3$; OD, outer diameter; ID, inner diameter.

potential by filling the resolution and imaging depth gap between the ultrasonic elastography and OCE.

Methods and materials

Ultrasonic transducer design and experimental setup

The schematic and a photograph of the experimental setup are shown in *Figure 1*. A focused 4 MHz large aperture ring shaped transducer and a 40 MHz unfocused small aperture needle transducer were designed and fabricated in this study. The general design parameters of these two transducers are listed in *Table 1*. The 4 MHz ultrasonic transducer was made of modified Pb(Zr,Ti)O_3 (PZT) ceramic dedicated for high power applications. This focused ring shaped transducer has an outer diameter (OD) of 30 mm, an inner diameter (ID) of 10 mm, and a focal length of 30 mm. The 4 MHz transducer was responsible for inducing the periodically vibrational movement of the imaging sample under a square wave modulated driving RF signal. The single crystal Pb($Mg_{1/3}Nb_{2/3}$)-$PbTiO_3$ (PMN-PT), exhibiting outstanding electromechanical coupling coefficient and piezoelectric coefficients, was used to fabricate the unfocused 40 MHz detection transducer for tracking the vibrational movement of imaging sample. The general fabrication procedures of needle transducers were described in our previous study (23).

Before the imaging experiment, the needle transducer was inserted from the center hole of the excitation transducer and the two transducers were carefully aligned in a confocal manner along both axial and lateral direction under the guidance of hydrophone. This precise alignment allowed the maximum overlapping of the low frequency ultrasound excitation zone and the high frequency ultrasound detection zone. In the excitation system, the 4 MHz ring transducer was excited by a 100 Hz square-wave modulated RF signal with a duty cycle of 50% that was amplified to 80-100 V by a power amplifier. Meanwhile, the 40 MHz ultrasonic transducer was driven by 200 MHz bandwidth pulser/receiver (5900PR, Panametrics, Waltham, WA, U.S.) with a pulse repetition rate of 20 kHz. A 20 ms imaging window was applied to cover two period of the harmonic motion. The backscattered echo signals was amplified by 26 dB and filtered by a 10-100 MHz band-pass filter before being digitized by a 2 GHz sampling frequency digitizer (121G11U, DynamicSignals, Lockport, IL, USA). Digital filtering was then carried out to remove the influence of low frequency component of excitation beam. A normalized cross-correlation method was used to estimate the displacement by using the first A-line within the imaging window as the reference. The average peak to peak displacement values were mapped to the final image for all detected depths. To obtain a 2-D displacement map, the imaging subject was placed on a motorized stage with 50 μm step size and up to a scanning length of 4 mm along lateral direction. Finally, the displacement amplitudes of all detected depth at each scanning position were used to reconstruct the 2-D HMI image.

Phantom preparation

Three agar-based tissue mimicking phantoms comprising of silicon dioxide powder as the sound scatterers were fabricated to evaluate the performance of imaging system (24). Two types of phantom with agar (Agar A360-500, Fisher Scientific, USA) concentrations of 0.5% and 1.5% were

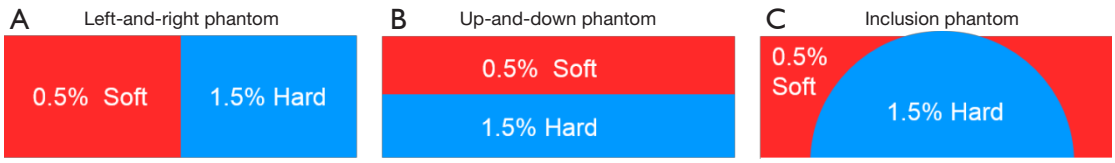

Figure 2 Geometry and composition illustration of (A) left-and-right phantom; (B) up-and-down phantom; and (C) inclusion phantom.

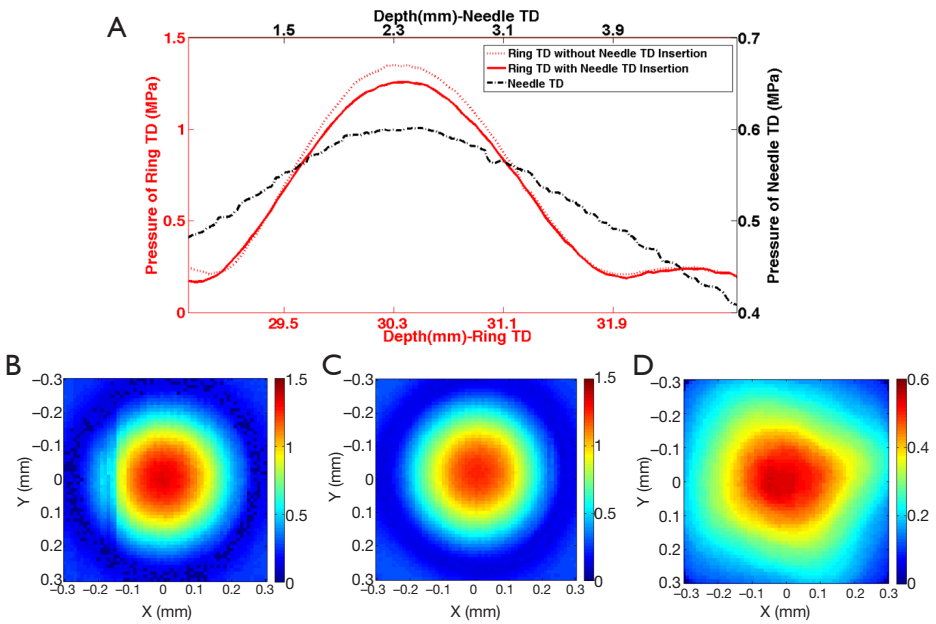

Figure 3 (A) 1D beam profile along the axial direction of 40 MHz needle transducer, and the 1D beam profile along the axial direction of 4 MHz ring transducer with and without needle transducer insertion; (B) 2D beam profile of 4 MHz ring transducer at focal plane without needle transducer insertion; (C) 2D beam profile of 4 MHz ring transducer at focal plane with needle transducer insertion; (D) 2D pressure profile of 40 MHz needle transducer.

fabricated to mimic the relatively soft and hard tissue, respectively. Same concentration of silicon dioxide powder (S5631, Sigma-aldrich, St. Louis, MO, USA) with particle size between 1 and 5 μm was added for echogenic enhancement. The three different types of phantom (left-and-right phantom, up-and-down phantom and circular inclusion phantom) were illustrated in *Figure 2A-C*, respectively. For the up-and-down phantom, the thickness of the upper layer was 0.5 mm. For the inclusion phantom, the radius of the cylindrical inclusion was about 2 mm.

Results and discussion

Transducer alignment confirmation and acoustic field characterization

The 4 MHz ring shape transducer was first placed in the water tank, and the 1D acoustic profile along axial direction (*Figure 3A*) and 2D acoustic beam profile (*Figure 3B*) at the focal plane were mapped with a hydrophone. Under the guidance of the hydrophone, the 40 MHz needle was inserted though the inner hole and carefully positioned to ensure confocal alignment of the two transducers along both axial and lateral direction. The acoustic profiles of ring transducer and needle transducer, as shown in *Figure 3A-D* were captured by the hydrophone with identical scanning range. A comparison of *Figure 3B,C* indicated that the inserted needle transducer did not appear to have any significant influence on the acoustic beam profile of the ring shape transducer, and there was only 7.6% peak pressure drop after inserting the needle transducer. The –6 dB beamwidth was used to determine the focal zone of the 4 MHz ring transducer during the one-way excitation process. With

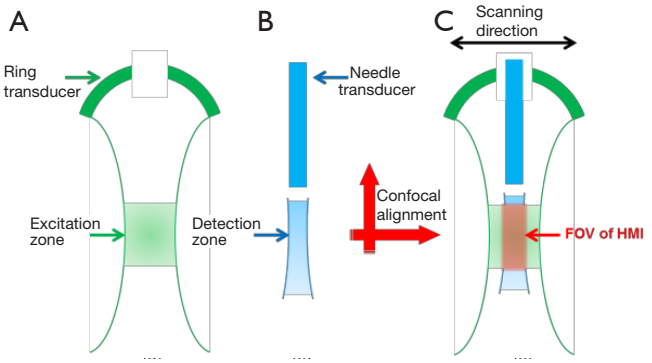

Figure 4 Illustration of confocal alignment procedures of transducers and the FOV determination HMI system. (A) Excitation zone of ring transducer; (B) detection zone of needle transducer; (C) FOV of HMI system: the overlapped region of excitation zone and detection zone. FOV, field of view; HMI, harmonic motion imaging.

the needle transducer inserted, the 4 MHz ring transducer had a focal zone of 0.36 mm laterally and 2.0 mm axially. As expected, the 40 MHz needle transducer had a square-shape 2D beam profile that matched with the square shape element. Since the transducer element is not focused, the axial beam profile exhibited relatively parallel characteristic to enlarge imaging depth. The –3 dB beamwidth was used to determine the focal zone of 40 MHz needle transducer during the two-way detection process. The 40 MHz needle transducer had a focal zone of 0.31 mm laterally and 4.3 mm axially. As shown in *Figure 3C,D*, it was observed that the 4 MHz ring transducer and the 40 MHz needle transducer were confocal in the lateral direction, where the focal zone of excitation transducer covered the focal zone of the needle transducer. Moreover, with the confocal alignment of the two transducers along axial direction (*Figure 3A*), the relatively parallel beam profile of 40 MHz needle transducer well covered the focal zone of the 4 MHz ring transducer. These results from hydrophone tests confirmed that the 4 MHz ring transducer and 40 MHz needle transducer had the exactly confocal alignment along both lateral and axial directions.

Figure 4 illustrates the confocal alignment procedures of the two transducers and the FOV determination of the HMI system. As shown in *Figure 4A*, the excitation zone of HMI system was determined by the –6dB beamwidth of 4 MHz ring transducer, where the ARF induced displacements were evenly distributed. Moreover, the detection zone (*Figure 4B*) was considered to be the –3 dB beamwidth (corresponding to –6 dB for two-way pulse-echo) of 40 MHz transducer, within which the detection transducer had similar imaging capability. To determine the FOV of HMI system, the detection zone should fall into the excitation zone with uniformly distributed ARF in the lateral direction so as to ensure the accuracy of the HMI. Furthermore, along the axial direction, the detection zone should cover the excitation zone so that the sensitivity of the HMI was enhanced since all of the particle motions induced by the ARF could be monitored at each imaging depth. Therefore, under the precise confocal alignment of excitation transducer and detection transducer, the effective FOV of this HMI system was the overlapping region of the excitation zone and the detection zone (indicated by the red arrow in *Figure 4C*), which was 29.5-31.5 mm away from the 4 MHz ring transducer surface and 1.5-3.5 mm away from the 40 MHz needle transducer surface. During the HMI experiment, the imaging subject was placed within this region to ensure the sensitivity and accuracy of HMI imaging system.

Several confocal dual-element transducer designs have been reported previously for high resolution ARFI imaging (22) and acoustic angiography (25), but they all exhibit the disadvantages of misalignment of the two transducer elements, which result in a downgraded sensitivity and decreased imaging FOV. Moreover, the high frequency detection transducer and the low frequency excitation transducer have the same working distance in these designs, which significantly downgrades the sensitivity and FOV of the high frequency detection transducer due to the higher attenuation of higher frequency ultrasound. Therefore, the unique combination of a focused ring transducer and an unfocused needle transducer not only allowed for the precise confocal alignment of the two transducers in both axial and lateral direction to enhance the sensitivity, but also effectively decreased the attenuation of the detection ultrasound beam by adjusting their working distance to enlarge the FOV of this HMI system.

Phantom imaging

The 0.5% concentration agar phantom and 1.5% concentration agar phantom were firstly placed inside the FOV separately to perform HMI at one location, where the ARF induced harmonic motion based displacements were assumed to be equally distributed along the axial direction inside each homogenous phantom. *Figure 5A* shows the estimated dynamic displacement curves of 0.5% agar

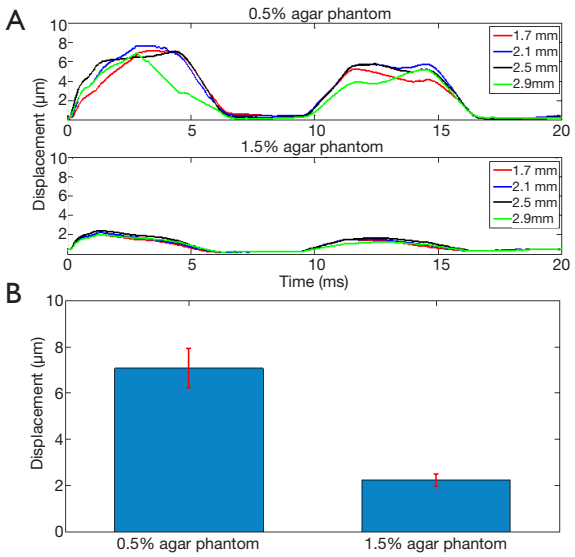

Figure 5 (A) Dynamic displacement curves within 20 ms imaging window of 0.5% agar phantom and 1.5% agar phantom at the axial depth of 1.7, 2.1, 2.5 and 2.9 mm; (B) average amplitudes of harmonic motion of the 0.5% agar phantom and 1.5% agar phantom along the axial direction.

phantom and 1.5% agar phantom at the axial depths of 1.7, 2.1, 2.5 and 2.9 mm. Within the 20 ms imaging window, two periods of harmonic motion (100 Hz modulation frequency) were tracked in both phantoms. It was observed that the dynamic displacement curves exhibited a small variance along the imaging depth. As shown in *Figure 5B*, the average harmonic motion amplitudes along the axial direction of FOV for the 0.5%-agar phantom and 1.5%-agar phantom were 7.08±0.86 and 2.23±0.26 μm, respectively. The capability of the HMI imaging system to provide distinguishable amplitudes of the harmonic motion based displacements within the two phantoms suggests that it can reliably discern the materials of varying stiffness within the FOV.

A total of 80 A-lines 50 μm apart from each other were used to reconstruct the B-mode image and the corresponding displacement map (HMI image) with an imaging region of 2 mm × 4 mm. *Figure 6* shows the B-mode images of the three types of phantoms (left-and-right, up-and-down, inclusion) and the corresponding HMI images. It was observed that the regions with different stiffness exhibited a homogenous echogenicity in the B-mode images, and the boundaries between which (indicated by the red dotted lines) could not be easily distinguished (except for the up-and-down phantom, in which the bright boundary was caused by the precipitation of silicon dioxide powder). On the other hand, the HMI images provide a clear visualization of the regions with different stiffness. The relative stiffness of the phantom was calculated and mapped to different colors. The red color and blue color indicate the lower stiffness with larger displacements and higher stiffness with smaller displacements, respectively. These phantom results suggest that the high resolution HMI system has the great potential to differentiate the tissue components with different biomechanical properties by mapping the relative stiffness to the structural image.

To further evaluate the performance of the high resolution HMI system, the imaging results of left-and-right phantom and up-and-down phantom were used to quantify the actual lateral resolution and axial resolution of this imaging technique, accordingly. The displacement curves along the lateral direction at the different axial locations (2.1, 2.3, 2.5, 2.7, and 3.0 mm) of the left-and-right phantom, plotted in *Figure 7A*, indicate that the displacement variation tendency matched favorably with the actual stiffness distribution of the phantom. The displacements were uniformly distributed within the left part and right part with a transition region in the middle. The displacement curves along the axial direction at different lateral locations (0.75, 1.75, 2.00, 2.75 and 3.50 mm) of the up-and-down phantom are plotted in *Figure 7B*, and a similar trend of displacements distribution is observed compared with the left-and-right phantom. The two corresponding averaged displacement curves are given in *Figure 7C,D*, and both fitted with a sigmoid function for resolution evaluation based on the standards reported previously (22,26). The 20% to 80% transition regions in the two fitting curves were used to quantify the axial and lateral resolution of this imaging system. The estimated the lateral and axial resolutions of this HMI system were 314 and 133 μm, respectively.

Theoretically, the lateral resolution in elastography is limited by the beamwidth of the detection transducer without dependence on cross-correlation window size. The estimated lateral resolution (314 μm) of this imaging system matches the measured –3 dB beamwidth (310 μm) of the detection transducer. The pulse width and the cross-correlation window size together determine theoretical axial resolution in elastography. In this study, the pulse width of 40 MHz detection transducer was 75 μm that was smaller than the chosen cross-correlation window size of 147 μm. The estimated axial resolution of 154 μm is in reasonably

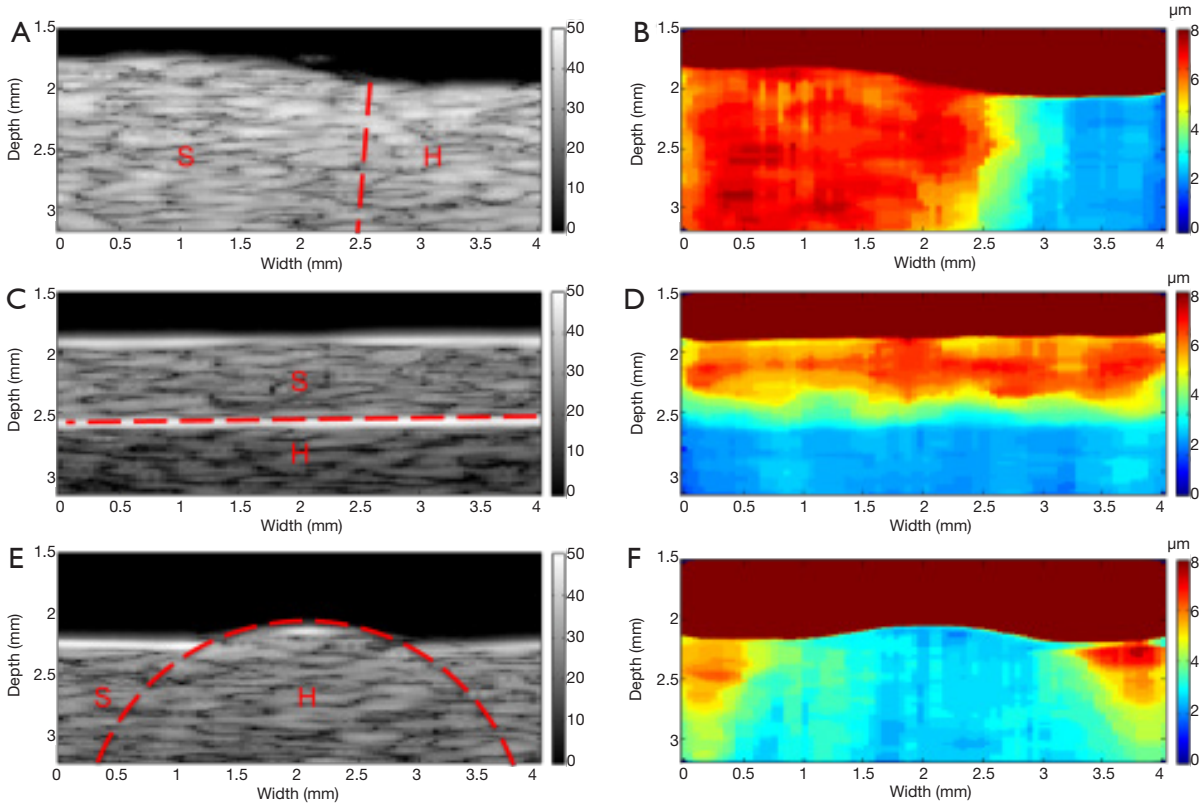

Figure 6 B-mode image (A) and its corresponding high resolution HMI image (B) of left-and-right phantom. B-mode image (C) and its corresponding high resolution HMI image (D) of up-and-down phantom. B-mode image (E) and its corresponding high resolution HMI image (F) of left-and-right phantom. The red dashed lines in the B-mode image represent the boundary estimated from the corresponding HMI image. S, soft 0.5%-agar phantom; H, hard 1.5%-agar phantom. HMI, harmonic motion imaging.

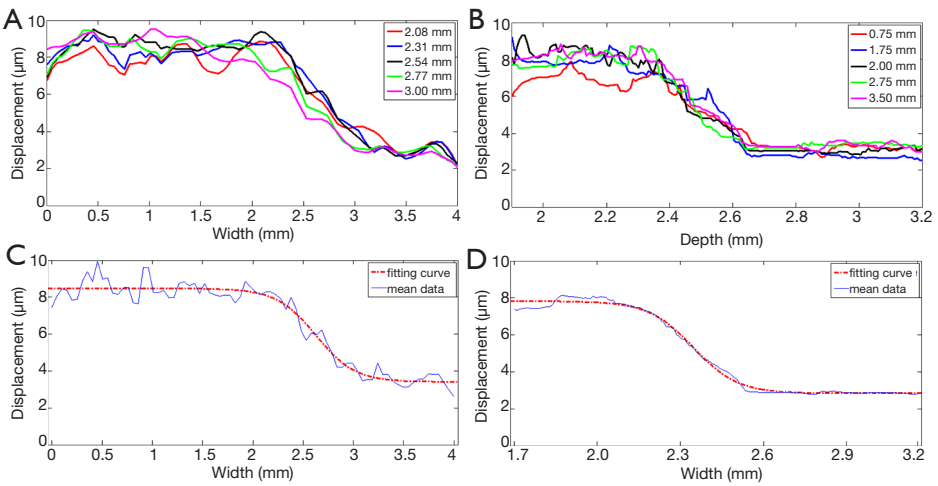

Figure 7 (A) Displacement curves of left-and-right along the lateral direction at the axial location of 2.08, 2.31, 2.54, 2.77 and 3.00 mm; (B) displacement curves of up-and-down phantom along the axial direction at the axial location of 0.75, 1.75, 2.00, 2.75 and 3.50 mm; (C) averaged displacement curves of left-and-right along the lateral direction with fitting curve; (D) averaged displacement curves of up-and-down phantom along the axial direction with fitting curve.

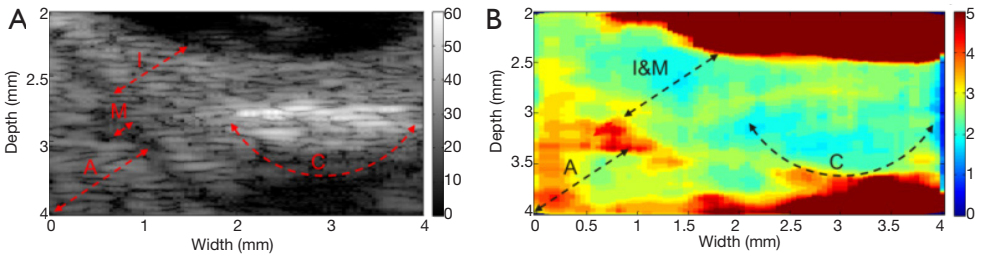

Figure 8 B-mode image (A) and its corresponding high resolution HMI image (B) of a section of human atherosclerosis coronary artery. I, intima layer; M, media layer; A, adventitia layer and surrounding tissue; C, calcified plaque; HMI, harmonic motion imaging.

agreement with the cross-correlation window size that is the major determiner of axial resolution in this study.

Ex vivo human coronary artery image

Finally, to demonstrate the feasibility of utilizing this high resolution HMI system to image and characterize the biomechanical properties of artery tissue, *ex vivo* HMI of a section of post-mortem atherosclerotic human coronary artery was performed. The human coronary artery was prepared and immersed in phosphate-buffered saline (PBS) solution during the imaging process. The B-mode image reveals (*Figure 8A*) that irregular thickening intima layer indicated by arrow I, the thin echolucent media layer indicated by arrow M, and the adventitia layer with surrounding tissue indicated by arrow A. A large calcified lesion, indicated by arrow C, is identified as a strong echogenicity region with acoustic shadowing. Even though the high frequency B-mode image is able to provide detailed structural information of the coronary artery, it cannot directly assess the biomechanical information of the artery tissue. The high resolution HMI image of the coronary artery is shown in *Figure 8B*. In the HMI image, the adventitia layer can be clearly discerned from the intima-media layer with higher displacement amplitude under the excitation, which agrees with fact that intima-media layers are stiffer than the adventitia layer (27). As expected, the calcification region exhibits a much smaller displacement than the adventitia region on the left and the intima layer above, which shows that the stiffness of calcified plaque is higher than the surrounding vascular tissue. The high resolution HMI image is able to provide the point-to-point stiffness mapping of the coronary artery, which is in reasonable agreement with the pathological information provided by the B-mode image.

These results demonstrate that the high resolution HMI is a promising ultrasound elastographical technique for tissue biomechanical property characterization at a small scale. Owing to the unique confocal alignment of the low frequency excitation transducer and the high frequency detection transducer, the lateral resolution and axial resolution of HMI are significantly improved. The spatial resolution of this HMI system can be further improved by using a higher frequency and smaller aperture detection transducer; however, the trade-off between the imaging resolution and size of FOV should be carefully considered during optimization. Using the similar excitation method, the recently developed resonant ARF-OCE has successfully provided resonant frequency specific contrast to the elastography image by sweeping the excitation frequency (21). This method can also be implemented on this high resolution HMI system to enhance the tissue biomechanical property characterization, which serves as an additional preponderance of HMI over the traditional ARFI imaging.

Conclusions

In this study, a high resolution HMI technique is developed to accurately distinguish imaging subjects with varying stiffness at a small scale. A 4 MHz focused ring shape transducer was designed to generate periodic ARF and induce the vibrational movements of sample in an efficient manner. Meanwhile, a 40 MHz unfocused needle transducer was used to track the movement and quantify the relative stiffness. The acoustic beams of two ultrasonic transducers were precisely aligned into confocal configuration to provide an effective FOV of 2 mm. The measured lateral and axial resolutions of HMI system were 314 and 154 μm, respectively. The feasibility of this HMI system on differentiating materials with different stiffness was validated on three different agar-based tissue-mimicking phantoms. These results demonstrate that the high resolution HMI is able to accurately map the stiffness distribution onto the structural ultrasound B-mode image.

The HMI of *ex vivo* human atherosclerosis coronary artery is able to determine the layer-specific pathological structure and identify the calcified plaque based on the biomechanical properties of the coronary artery. The high resolution HMI appears to offer a promising ultrasound-only technology for charactering tissue biomechanical properties at the microstructural level to improve the image-based diseases diagnosis in multiple clinical applications.

Acknowledgements

This work is supported by the National Institute of Health under grant P41-EB002182, R01-EB10090 and 1R01EY021529. The authors acknowledge Dr. Zhongping Chen and Ms. Jiawen Li for providing tissue samples. The authors also wish to thank individuals who donate their bodies and tissues for the advancement of education and research.

Disclosure: The authors declare no conflict of interest.

References

1. Parker KJ, Doyley MM, Rubens DJ. Imaging the elastic properties of tissue: the 20 year perspective. Phys Med Biol 2011;56:R1-R29.
2. Cheng GC, Loree HM, Kamm RD, Fishbein MC, Lee RT. Distribution of circumferential stress in ruptured and stable atherosclerotic lesions. A structural analysis with histopathological correlation. Circulation 1993;87:1179-87.
3. Garra BS, Cespedes EI, Ophir J, Spratt SR, Zuurbier RA, Magnant CM, Pennanen MF. Elastography of breast lesions: initial clinical results. Radiology 1997;202:79-86.
4. Ophir J, Céspedes I, Ponnekanti H, Yazdi Y, Li X. Elastography: a quantitative method for imaging the elasticity of biological tissues. Ultrason Imaging 1991;13:111-34.
5. Wells PN, Liang HD. Medical ultrasound: imaging of soft tissue strain and elasticity. J R Soc Interface 2011;8:1521-49.
6. Nightingale KR, Palmeri ML, Nightingale RW, Trahey GE. On the feasibility of remote palpation using acoustic radiation force. J Acoust Soc Am 2001;110:625-34.
7. Nightingale K. Acoustic Radiation Force Impulse (ARFI) Imaging: a Review. Curr Med Imaging Rev 2011;7:328-39.
8. Fatemi M, Greenleaf JF. Ultrasound-stimulated vibro-acoustic spectrography. Science 1998;280:82-5.
9. Bercoff J, Tanter M, Fink M. Supersonic shear imaging: a new technique for soft tissue elasticity mapping. IEEE Trans Ultrason Ferroelectr Freq Control 2004;51:396-409.
10. Sarvazyan AP, Rudenko OV, Swanson SD, Fowlkes JB, Emelianov SY. Shear wave elasticity imaging: a new ultrasonic technology of medical diagnostics. Ultrasound Med Biol 1998;24:1419-35.
11. Maleke C, Luo J, Gamarnik V, Lu XL, Konofagou EE. Simulation study of amplitude-modulated (AM) harmonic motion imaging (HMI) for stiffness contrast quantification with experimental validation. Ultrason Imaging 2010;32:154-76.
12. Vappou J, Maleke C, Konofagou EE. Quantitative viscoelastic parameters measured by harmonic motion imaging. Phys Med Biol 2009;54:3579-94.
13. Maleke C, Konofagou EE. Harmonic motion imaging for focused ultrasound (HMIFU): a fully integrated technique for sonication and monitoring of thermal ablation in tissues. Phys Med Biol 2008;53:1773-93.
14. Maleke C, Pernot M, Konofagou EE. Single-element focused ultrasound transducer method for harmonic motion imaging. Ultrason Imaging 2006;28:144-58.
15. Righetti R, Srinivasan S, Ophir J. Lateral resolution in elastography. Ultrasound Med Biol 2003;29:695-704.
16. Righetti R, Ophir J, Ktonas P. Axial resolution in elastography. Ultrasound Med Biol 2002;28:101-13.
17. Wang PK, Kirkpatrick SJ, Hinds MT. Phase-sensitive optical coherence elastography for mapping tissue microstrains in real time. Applied Physics Letters2007;90:164105-164105-3.
18. Qi W, Li R, Ma T, Kirk Shung K, Zhou Q, Chen Z. Confocal acoustic radiation force optical coherence elastography using a ring ultrasonic transducer. Appl Phys Lett 2014;104:123702.
19. Qi W, Chen R, Chou L, Liu G, Zhang J, Zhou Q, Chen Z. Phase-resolved acoustic radiation force optical coherence elastography. J Biomed Opt 2012;17:110505.
20. Nguyen TM, Song S, Arnal B, Huang Z, O'Donnell M, Wang RK. Visualizing ultrasonically induced shear wave propagation using phase-sensitive optical coherence tomography for dynamic elastography. Opt Lett 2014;39:838-41.
21. Qi W, Li R, Ma T, Li J, Kirk Shung K, Zhou Q, Chen Z. Resonant acoustic radiation force optical coherence elastography. Appl Phys Lett 2013;103:103704.
22. Shih CC, Huang CC, Zhou Q, Shung KK. High-resolution acoustic-radiation-force-impulse imaging for assessing corneal sclerosis. IEEE Trans Med Imaging 2013;32:1316-24.

23. Ma T, Zhang X, Chiu CT, Chen R, Kirk Shung K, Zhou Q, Jiao S. Systematic study of high-frequency ultrasonic transducer design for laser-scanning photoacoustic ophthalmoscopy. J Biomed Opt 2014;19:16015.
24. Hall TJ, M. Bilgen M, Insana MF, Krouskop TA. Phantom materials for elastography. IEEE transactions UFFC 1997;44:1355-64.
25. Gessner RC, Frederick CB, Foster FS, Dayton PA. Acoustic angiography: a new imaging modality for assessing microvasculature architecture. Int J Biomed Imaging 2013;2013:936593.
26. Rouze NC, Wang MH, Palmeri ML, Nightingale KR. Parameters affecting the resolution and accuracy of 2-D quantitative shear wave images. IEEE Trans Ultrason Ferroelectr Freq Control 2012;59:1729-40.
27. Holzapfel GA, Sommer G, Gasser CT, Regitnig P. Determination of layer-specific mechanical properties of human coronary arteries with nonatherosclerotic intimal thickening and related constitutive modeling. Am J Physiol Heart Circ Physiol 2005;289:H2048-58.

Cite this article as: Ma T, Qian X, Chiu CT, Yu M, Jung H, Tung YS, Shung KK, Zhou Q. High-resolution harmonic motion imaging (HR-HMI) for tissue biomechanical property characterization. Quant Imaging Med Surg 2015;5(1):108-117. doi: 10.3978/j.issn.2223-4292.2014.11.27

